Spatial and Temporal Variation of Mars South Polar Ice Composition from Spectral Endmember Classification of CRISM Mapping Data

S. F. A. Cartwright[1,2] W. M. Calvin[3], F. P. Seelos[2], and K. D. Seelos[2]

[1]Department of Geological Sciences, Laboratory for Atmospheric and Space Physics, University of Colorado, Boulder, CO, USA

[2]Johns Hopkins University Applied Physics Laboratory, Laurel, MD, USA

[3]Department of Geological Sciences and Engineering, University of Nevada, Reno, NV, USA

Corresponding author: Samuel Cartwright (samuel.cartwright@colorado.edu)

Key Points:

- Variable mixtures of CO_2 and H_2O ice with dust are linked to the formation of south polar climate records.
- To better understand these mixtures, we mapped 12 endmembers across multispectral data spanning 6 south polar summers.
- We made a series of mosaics to explore compositional variation in both seasonal and residual ice deposits.

Abstract

Multispectral mapping data from the Compact Reconnaissance Imaging Spectrometer for Mars (CRISM) provide a unique opportunity to characterize south polar ice deposits at higher spectral sampling, spatial resolution, or spatiotemporal coverage than previous work. This new perspective can help to constrain the nature and distribution of different mixtures of CO_2 ice, H_2O ice, and dust that influence the formation, evolution, and preservation of Mars climate records. We processed 1103 CRISM observations spanning southern summer of six Mars Years (MY) through a combination of *k*-means clustering and random forest classification. Using a set of 12 spectral endmembers directly tied to previous work with high-resolution CRISM targeted data, we made a series of temporally restricted mosaics showing surface spectral variation over time. The mosaics show the effects of the MY 28 dust storm on the removal of the seasonal CO_2 ice cap that year and reveal how this process differed from the years that followed. A mosaic showing residual ice surfaces displays broad agreement with previous compositional maps while resolving new details in the distribution of H_2O ice-rich material around the periphery of the bright CO_2 ice cap. By showing how surface composition varies across a broad swath of the south polar region though time, the endmember set and classified mosaics produced in this work can provide critical context for future studies of the dynamic processes that shape south polar ice deposits.

Plain Language Summary

At the south pole of Mars, different mixtures of CO2 ice, water ice, and dust on the surface influence interactions with the atmosphere. These influences affect how polar ice deposits are formed, how they change over time, and how they are preserved as records of past climates. Existing maps of ice and dust in the region have limitations in how accurately they can describe mixtures and how much detail they can show on the ground. Using data from an orbiting spectrometer that measures sunlight reflected from the surface, we made new maps that reveal important details not seen in previous work. For example, these maps show how surface composition changes through time, which can be used to study CO2 frost that forms on the surface every winter and is removed in the summer. We observe how a dust storm in one year affected the composition and/or thickness of seasonal frost compared to other years. The maps also reveal how composition varies in different permanent ice deposits. Compared to previous work, it is easier to see how CO2 ice and dust are mixed with water ice in enigmatic exposures that may be linked to the formation of new climate records.

1 Introduction

Both the present dynamics of Mars's climate and its evolution over the past tens of millions of years are preserved in the icy stratigraphy of the planet's south pole (Byrne, 2009). This has drawn an evergrowing body of observation and related research into the processes that have shaped this fascinating region (Smith, 2022; Landis et al., 2023). A detailed understanding of surface composition is key to interpreting the climate history that these landscapes preserve, specifically how the formation and evolution of ice deposits are influenced by variable mixtures of CO_2 ice, H_2O ice, and settled atmospheric dust. In this paper, we present the first comprehensive study of south polar spectral variation as captured by multispectral mapping data from the Compact Reconnaissance Imaging Spectrometer for Mars (CRISM, Murchie et al.,

2007). We turned to these data for two reasons described below that together provide a unique opportunity to explore connections between south polar ices and the climate history of Mars.

First, CRISM mapping data provide a view of the south polar region that can place the compositional framework outlined by Cartwright et al. (2022) in a broader spatial context. In that paper, we used hyperspectral CRISM data at 18–36 m/pixel to identify and map a set of 21 spectral endmembers at over 100 sites distributed across the south pole. There are two key deposits explored in that work: the ~4 km-thick dome of interbedded water ice and dust known as the South Polar Layered Deposits (SPLD, see Plaut et al., 2007) and the overlying South Polar Residual Cap (SPRC). We further divide the SPRC into the high-albedo Residual CO_2-ice Deposits (RCD, see Thomas et al., 2016) and the moderate-albedo Peripheral Water-ice Deposits and Outlier Water-ice Deposit (PWD and OWD, respectively; see Piqueux et al., 2008). Exposures of these units are labeled in Figure 1 and the reader is referred to Cartwright et al. (2022) for a table with additional unit descriptions.

The endmember classified maps of CRISM targeted data reveal variations in the nature of seasonal CO_2 frost cover (see Prettyman et al., 2009) within and between Mars Years (MYs, Piqueux, Byrne, et al., 2015). In particular, following the large dust event in MY 28 (Calvin et al., 2017; Piqueux, Kleinböhl, et al., 2015), seasonal frost signatures are more persistent within the SPRC compared to other years. In unfrosted residual ice exposures, the classified maps show unexpected complexity in ice mixtures, including CO_2 ice signatures that remain in low-albedo material well into late southern summer. Together these results provide a compelling window into the diversity and dynamism of south polar ice exposures, but this view is ultimately limited by the restricted spatial sampling of high-resolution CRISM maps, which only cover a fraction of the total area of the SPRC. By expanding this work with multispectral CRISM data that offer more complete coverage of these terrains through time, we can assess the accuracy of the existing compositional framework and potentially improve it with new insights.

Second, CRISM mapping data can bridge a gap in understanding between existing maps of south polar composition. While the presence of CO_2 and H_2O ices in the region had been understood for decades (e.g., Kieffer, 1979; Murray et al., 1972) their associations with different surface units were unclear until the arrival of the Observatoire pour la Minéralogie, l'Eau, les Glaces et l'Activité (OMEGA; Bibring, Soufflot, et al., 2004). With 352 spectral channels sampling 0.38–5.1 μm, OMEGA data proved capable of distinguishing varied mixtures of ice and dust across the SPRC and in particular, highlighted the presence of water ice (Bibring, Langevin, et al., 2004; Douté et al., 2007; Langevin et al. 2007). However, the amount of detail captured by these maps is limited by the 700–2000 m/pixel resolution of south polar OMEGA observations. An alternative perspective on Mars surface composition is provided by the Thermal Emission Imaging System (THEMIS; Christensen et al., 2004), which offers a higher spatial resolution of 100 m/pixel. This allowed Titus et al. (2003) to first identify water ice within the SPRC, and later, for Piqueux et al. (2008) to map exposures of water ice more completely. However, with 10 channels covering 6.8–14.9 μm, THEMIS can only identify thermal signatures generally indicative of ice and dust mixtures and cannot characterize them further.

Owing to its spatial resolution of 90–180 m/pixel and spectral sampling of 55 channels in the short-wave infrared (SWIR) from 1.00–3.93 μm, CRISM mapping data can distinguish varied mixtures of CO_2 ice, H_2O ice, and dust with fidelity similar to OMEGA while also resolving their exposure with spatial detail similar to THEMIS. Maps of south polar composition

from CRISM mapping data could therefore bridge the gap between existing views of compositional variation offered by these instruments.

While hyperspectral CRISM data have helped to revolutionize our understanding of Mars surface mineralogy, multispectral mapping data have been comparatively under-utilized. This is especially true in the south polar region, where the last detailed study of these data was only able to cover the first MY of observation (Brown et al., 2010). To address this problem, we have conducted a comprehensive study of CRISM SWIR mapping data at the south pole during the southern summer of each of the 6 MYs for which data were acquired. In this paper, we (a) describe the process of mapping spectral endmembers across the south polar dataset based on those identified in Cartwright et al. (2022), (b) present results from compiling the classified data into a series of temporally restricted mosaics, (c) investigate spatio-temporal trends in the composition of seasonal and residual ice deposits that those mosaics reveal, and (d) discuss how these findings compare to previous work and the broader implications they have for the formation and evolution of south polar ices.

2 Data

2.1 CRISM's Spectral Perspective

The endmember extraction and mapping presented in Cartwright et al. (2022) leveraged CRISM targeted data, which are observations that rely on the instrument gimbal to point at a specific site on the planet's surface. While these views provide exceptionally high spatial and spectral resolutions (18 or 36 m/pixel, 438 SWIR channels), their footprints are accordingly limited to a maximum area of about 10×20 km. Total coverage of the 167 endmember maps produced in the previous work is therefore only ~5% of the total surface area of ice deposits comprising the SPRC. However, CRISM offers a complimentary dataset in the form of mapping data, which are acquired in pushbroom configuration to image broad swaths of the surface. These data trade larger areas (10×500+ km) for more limited spatial and spectral sampling (90 or 180 m/pix, 55 or 154 SWIR bands). These qualities enable CRISM mapping data to be compiled into mosaics that show spectral variation at regional scales (Viviano et al., 2020; Seelos et al., 2023), which in turn makes it possible to fill gaps in understanding left by previous compositional maps.

There are two observing modes of CRISM mapping data relevant to this study which share a spectral sampling of 55 SWIR channels (sufficient to capture key CO_2 and H_2O ice absorption features), but differ in spatial resolutions and temporal sampling (Fig. 1). Multispectral Survey (MSP) observations show the surface at 180 m/pixel resolution and were acquired throughout the same period as targeted SWIR observations (MY 28–33). When taken in aggregate, MSP data provide nearly universal coverage of the RCD during southern summer. The temporal sampling of Multispectral Window (MSW) data is comparatively limited in that it only captures the southern summer of MY 28, which in turn leads to less comprehensive spatial coverage. However, MSW mapping strips image the surface at 90 m/pixel, which allows them to resolve details around large erosional mesas on the surface of the RCD and narrow exposures along its margins.

2.2 Data Coverage and Temporal Sampling

To capture spatial variation in and around the SPRC, we ran endmember processing on all MSP and MSW strips that cover the region below 81ºS and between -135–60ºE. We restricted

this set to only observations that span from southern summer solstice to southern autumnal equinox, which corresponds to an aerocentric solar longitude (L_S) of 270–360º. We did not place any restrictions on the local time of acquisition for the data, which span from ~14:00–2:00. Spatial and temporal trends in the final set of 983 MSP and 120 MSW observations are illustrated in Figure 1. The greatest density of coverage was acquired in MY 28 and 29 (particularly with MSP data) and almost any temporal slice through the dataset greatly expands on the corresponding coverage offered by targeted data observations. However, it is important to note that spatial and temporal coverage (in terms of sampled L_S) varies significantly between MYs, with particularly sparse coverage from MY 30–33. This means that the most effective inter-annual comparisons can be made between MY 28 and 29, though some L_S ranges offer opportunities to compare up to four MYs.

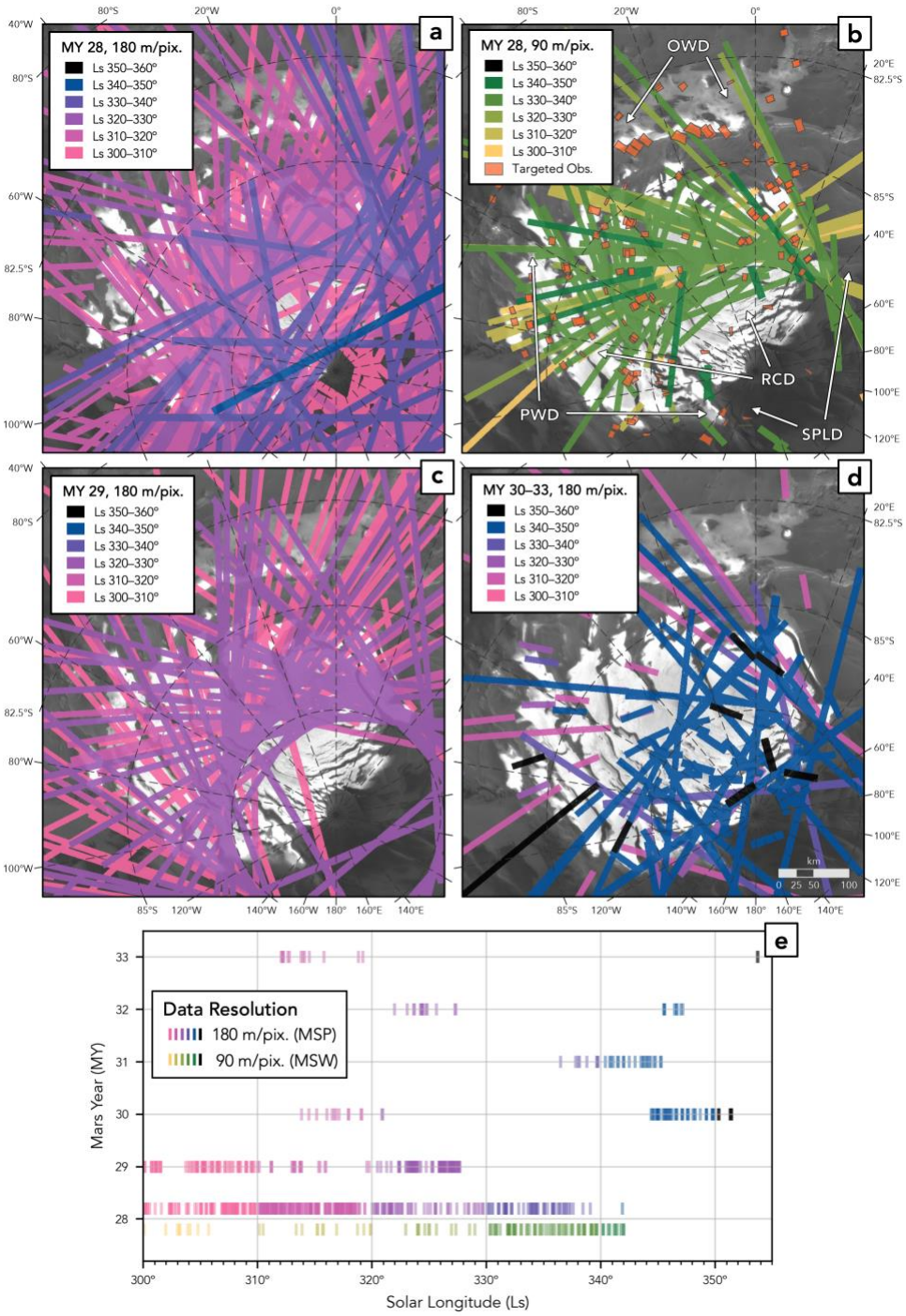

Figure 1. Spatial and temporal coverage of south polar CRISM mapping data used in this study. Observations that fall within 10º bins of solar longitude (L_S) are rendered with the same color while two color gradients are used to differentiate observing modes and their associated spatial resolutions: pink-blue for Multispectral Survey (MSP, 180 m/pixel) and yellow-green for Multispectral Window (MSW, 90 m/pixel). Note that while our analyses span L_S >270º, only L_S >300º are presented here for clarity. (**a**) MSP coverage in Mars Year (MY) 28. (**b**) MSW coverage in MY 28 and footprints of CRISM targeted data used in Cartwright et al. (2022) that span L_S 300–360º in MY 28–33. Labels note exposures of the key ice deposits described in the

text: high albedo Residual CO_2-ice Deposits (RCD), moderate albedo Peripheral Water-ice Deposits (PWD) and Outlier Water-ice Deposit (OWD), and low albedo South Polar Layered Deposits (SPLD). (**c**) MSP coverage in MY 29. (**d**) MSP coverage across MY 30–33. (**e**) Plot of temporal sampling in which each tick is a single observation, colored according to L_S bin and plotted by the MY and L_S at which it was acquired. A vertical offset is used to separate the two observing modes in MY 28 while a slight transparency highlights times of denser coverage.

2.3 Data Processing and Reduction

Pre-processing of the data used in this study was based on a new workflow developed for the creation of next-generation CRISM map mosaic products (Seelos et al., 2023). While the pipeline is designed to use a network of radiometrically calibrated reference strips to reconcile differences between data, this reference network is not available at the poles. We therefore chose to focus solely on the strip-independent processing steps that are part of this workflow and which are based on corresponding state-of-the-art corrections used to generate CRISM Targeted Empirical Records (TERs). In this portion of the workflow, each mapping data strip is passed through ratio shift, photometric, atmospheric, and spectral smile corrections to produce the clearest possible view of surface spectral variation. The reader is referred to Murchie et al. (2016) for additional details on each of these corrections.

The map-projected data were then converted to *numpy* arrays for endmember analyses. This process included filtering each spectrum to remove and interpolate across bad bands; four channels around the SWIR filter boundary and longest wavelengths had consistently suspect radiometry and were removed. The spectra were then normalized by the reflectance measured at 1.330 μm (the R1330 parameter described in Viviano-Beck et al., 2014); this method differs slightly from our work with targeted observations due to the more limited spectral sampling of mapping data.

3 Methods

3.1 Machine learning methods in previous work

The spectral endmembers and classified maps presented in Cartwright et al. (2022) were produced by applying versatile machine learning algorithms to CRISM targeted data. First, a set of candidate endmembers were identified from a subset of high-quality, representative observations using *k*-means clustering. This is an unsupervised learning technique that divides a set of *n* samples (e.g., CRISM spectra) into *k* clusters such that the variance between samples within each cluster is minimized (Arthur & Vassilvitskii, 2007). Those candidate endmembers were then mapped across the entire dataset using random forest classification. This is an ensemble learning method in which a large number of decision trees independently evaluate the features of a sample (e.g., a CRISM spectrum) and vote to assign it a classification (Breiman, 2001). These two methods proved useful in distilling compositional information from a large spectral dataset and yielded tightly constrained endmembers with spatially consistent classified maps. We therefore chose to leverage these tools again in expanding the work to CRISM mapping data. The reader is referred to Cartwright et al. (2022) for additional detail on the model parameters associated with these two methods and their implementations in the context of hyperspectral image data.

3.2 Initial classification attempt

The most straightforward approach to expanding on this work is to directly map the previously derived targeted data endmembers onto mapping data spectra. To do this, the training data used to build the original random forest model are simply subsampled from their native 438 SWIR channels to the set of 55 channels that are also sampled by MSP and MSW data. A new random forest model can then be trained with these spectra and used to classify individual pixels from mapping data strips. In practice, however, we found that this method produces two main types of misclassification: 1) along-track striping that indicates subsampled targeted data spectra do not capture noise unique to mapping data, and 2) inconsistent mapping of some water ice-rich endmembers that suggest the weaker CO_2 absorptions used to distinguish them are not captured by the random forest model.

3.3 New classification workflow

To address these misclassification issues, we developed a new workflow (Fig. 2) to generate the results presented in this paper. The key difference is that this workflow incorporates mapping data and its unique characteristics from the start to build a set of candidate endmembers which are then used as training data for the random forest classification model. We then correlate the mapping data-derived endmembers to the spectral features and surface expression of those derived from targeted data.

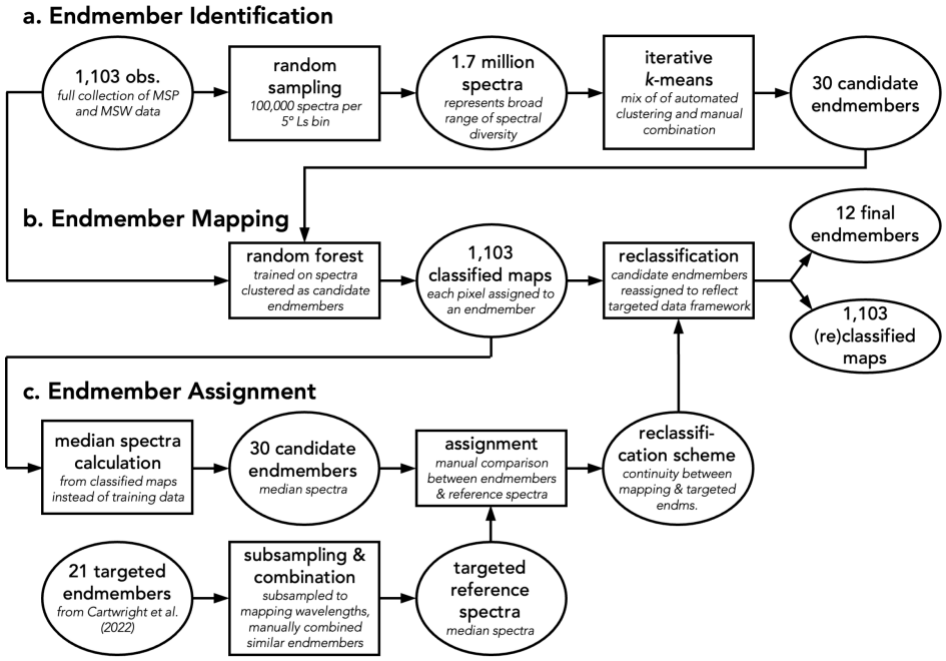

Figure 2. Workflow diagram of the methods used to (**a**) extract a set of candidate endmembers unique to south polar mapping data from CRISM, (**b**) map those endmembers across each

observation in the dataset, and (**c**) assign those endmembers to an appropriate reference spectrum derived from south polar CRISM targeted data presented in Cartwright et al. (2022).

3.3.1 Endmember identification with *k*-means clustering

To increase the efficiency of the *k*-means clustering procedure, we reduced the mapping dataset to a representative sampling. This was done by moving sequentially in 5° L_S bins between L_S 270–360°, making compilations of all the MSP and MSW observations acquired within each bin, and randomly sampling 10^5 pixels from each compilation. By aggregating the samples for each bin in which data were collected, we built a collection of 1.7 million spectra (equivalent to ~1% of the full dataset). This compilation offers a broad sampling of south polar terrains, but without the temporal sampling bias inherent in the south polar mapping dataset (Fig. 1e).

To avoid clustering results that were driven to local minima by unfiltered bad bands (see data filtering outlined in Section 2.3), we truncated the pixel compilation to remove all spectral channels at wavelengths longer than 2.6 µm. An iterative process of *k*-means clustering was then applied in which an initial set of 10 clusters were generated, their mean spectra were manually evaluated, and similar clusters were combined. Spectra assigned to each of the new, combined clusters were divided again by the *k*-means algorithm and evaluated. This process was repeated until all clusters could be distinguished by meaningful spectral differences, resulting in a set of 30 candidate endmembers (Fig. 2a). Despite the separability of the spectra in this set, it was understood that subsequent processing would necessarily reduce this to a collection of final endmembers no larger than the 21 identified with targeted data.

3.3.2 Endmember mapping with random forest

We trained the new mapping data-derived random forest model with a set of 1,500 randomly sampled spectra from each of the 30 candidate endmembers. We found that a forest with *ntree* = 1,000 and *mtry* = 10 was able to reduce the reported out-of-bag (OOB) error to 8.5%. The trained model was used to classify each of the ~17 million pixels across the collection of 1,103 MSP and MSW observations (Fig. 2b). Median spectra were then calculated for each of the 30 candidate endmembers that had been mapped.

3.3.3 Endmember correlation

The final step in the classification workflow was to assign each of the candidate mapping data endmembers to the most similar endmember derived from the targeted dataset, allowing for a one-to-one comparison of the results from the two investigations (Fig. 2c). First, the targeted data endmembers were downsampled to mapping data wavelengths to make a set of reference spectra. Then the strengths and combinations of absorption features in each of the 30 candidate endmembers were compared visually to the features present in the reference spectra. Candidate endmembers were then assigned to the best overall match to their spectral structure; additional details on this comparison process are presented in Supporting Information S1. The resulting reclassification scheme was used to reassign the random forest classification of each mapping data pixel to fit the compositional framework developed with targeted data. Lastly, a collection of 10^4 randomly sampled spectra were pulled for each of the endmembers to calculate the median spectrum along with other percentile statistics characterizing the degree of spectral variation.

3.4 Mosaic creation

To assess temporal changes within and between MYs, we generated a series of mosaics for 10º L_S bins across six southern summers. Mosaics were made by stacking endmember-classified mapping strips in ascending order of L_S; no manual editing, reconciliation of classification results between strips, or geodetic control were applied. Each product was exported at 180 m/pixel and in MY 28, combined MSP and MSW observations. Using these temporally restricted mosaics, we identified the L_S ranges in each MY that did not show endmembers associated with seasonal CO_2 frost. Mapping strips from those ranges were then compiled to generate a final mosaic that primarily shows residual ice. The mosaics were evaluated in GIS software in comparison to other remote sensing datasets like THEMIS and OMEGA compositional maps and a mosaic of Context Camera (CTX) data (Douté et al., 2007; Piqueux et al., 2008; Thomas et al., 2016).

4 Results

4.1 Endmember spectral characteristics

Endmembers in the Cartwright et al. (2022) framework span a wide range of apparent mixtures of ice and dust present at the south pole. To effectively show this variation, the endmembers were sorted by compositional gradients and each was named with an alphanumeric code indicating relative strengths of features associated with CO_2 ice (C/c), water ice (W/w), and dust (D/d). For example, Dc1 represents a spectrum dominated by dust signatures but with secondary CO_2 ice features. Numbers and color gradients indicate gradation towards the strength of a third component; for example, Dc3 displays stronger contributions from water ice than Dc1. The set of 12 endmembers now identified in mapping data inherits the colors and names used in the previous set, but with an appended “m” to indicate association with CRISM mapping data (e.g., Dc3m). Although not every one of the 21 targeted endmembers has an equivalent in the new set, the mapping data capture a similarly broad sampling of ice and dust mixtures.

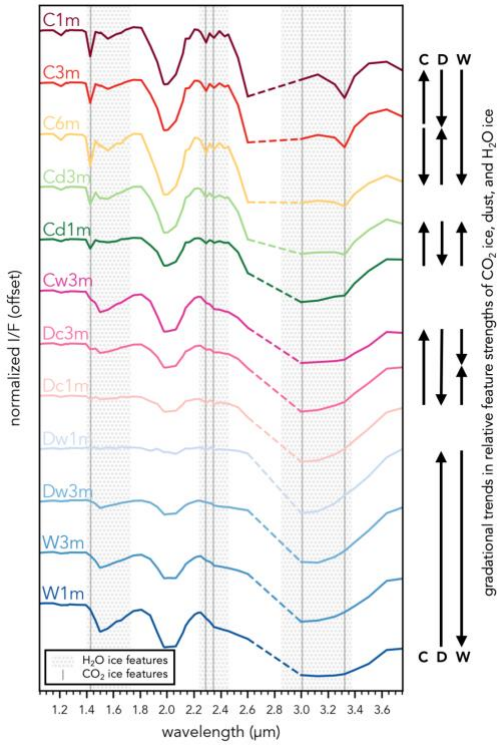

Figure 3. Median spectra of each endmember mapped across the multispectral mapping dataset with random forest classification. Dashed portions of spectra represent interpolation across the CRISM filter boundary. Arrows to the right of the plot indicate trends towards increasing feature strength for CO_2 ice, dust, and water ice.

The 12-endmember set (Fig. 3) includes a pure CO_2 ice spectrum (C1m, deep red) that grades towards increasing water ice contribution (C3m, red and C6m, yellow) evidenced by a strengthening of the 1.5 μm feature and suppression of albedo around 3.1 μm. As in the previous work, we found that this group of endmembers is closely associated with seasonal CO_2 frost (C1m) and residual CO_2 ice with likely sub-pixel contributions from water ice around erosional features (C6m). Also found in the set is a pure water ice spectrum (W1m, deep blue) that grades towards a nearly pure dust spectrum (Dw1m, pale blue). These endmembers are known to be associated with portions of the PDW/OWD and the SPLD, respectively. Other endmembers (shades of pink) indicate a more complex interplay of these mixing components in which a relatively weak but constant CO_2 ice absorption is found with dust (Dc1m), water ice (Cw3m), or an intermediate combination (Dc3m). Transitioning towards stronger CO_2 ice features (shades of green), other endmembers are similarly split between stronger dust (Cd1m) and water ice (Cd3m). Targeted data showed these pink and green endmembers to be associated with a wide variety of terrains around the SPRC and across L_S.

The only spectral type in this broad sampling that is apparently absent from the mapping data is one with exceptionally strong absorption features associated with both CO_2 ice and water ice. In targeted data, this endmember (Cw1) was found to be closely associated with the removal of seasonal frost over water ice-rich terrain. It is likely that either the narrow L_S range in which this late-stage removal occurs is not well sampled by the mapping dataset or that coarser spatial and spectral sampling are insufficient to adequately capture the phenomenon.

In comparison to spectra from targeted data endmembers, these mapping data endmembers have *stronger* CO_2 ice features in CO_2 ice-dominated spectra, but *weaker* H_2O ice features in H_2O ice-dominated spectra (see Fig. S3 in Supporting Information S1). Other trends are at play in mixtures, but most notably, Cw and Dc endmembers (shades of pink) have weaker CO_2 ice absorptions in mapping data. These trends point to potential differences in how ice on the surface is captured by CRISM mapping data and/or interpreted by our endmember extraction and mapping methods.

4.2 Temporal trends

Given its spatial and temporal coverage, the south polar mapping dataset captures a highly detailed view of how the planet's surface has changed across L_S and between MYs. One way to distill this wealth of information is through proportional bar plots like those shown in Figure 4. Here, all observations falling in 10º L_S bins were compiled and the mapped areas of each endmember in each observation were calculated. It is important to keep in mind that trends in CRISM's spatial and temporal sampling can limit the overall area and terrains covered in each L_S bin, and therefore, exact areas or individual L_S bins should not be over-interpreted. However, these plots do effectively illustrate broader temporal trends in surface composition by showing the relative proportions of each endmember mapped in temporal slices.

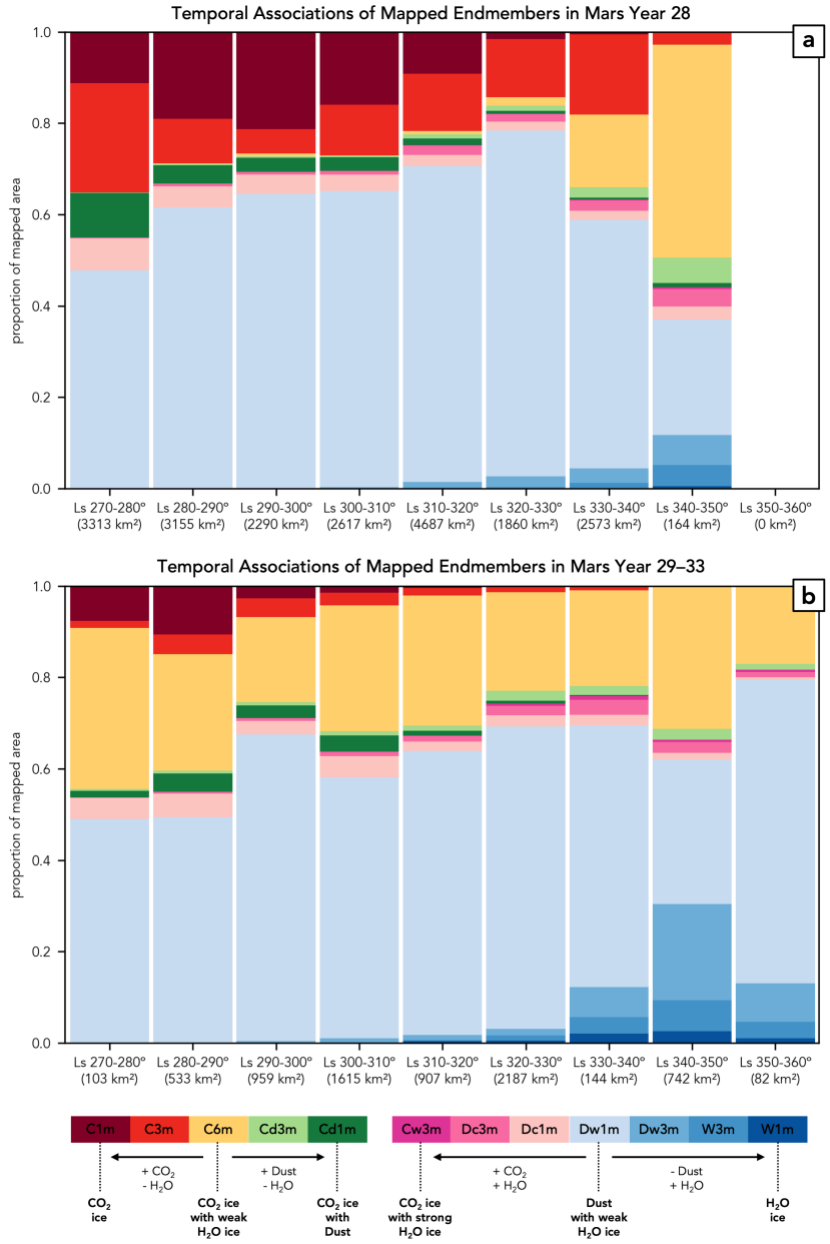

Figure 4. Mapped endmembers expressed as the proportion of total area covered by MSP and MSW observations in 10º L_S bins over the course of southern summer. This highlights temporal trends in the surface expression of endmembers within endmember groups, though the exact proportions in any particular column may be skewed by limits in spatial and temporal sampling illustrated in Figure 1. (a) Endmember proportions during MY 28 in which very CO_2 ice-rich endmembers (reds of C1m, C3m) are prevalent across L_S. (b) Endmember proportions during MY 29–33 that show comparatively stronger expression of a CO_2 ice-rich endmember with weak H_2O ice features (yellow of C6m).

These plots show that the expression of endmember groups will shift over the course of the summer to those with stronger water ice signatures. Specifically, a greater proportion of darker blues (W1m, W3m) will be found with light blue (Dw1m), more dark pinks (Cw3m,

Dc3m) than light pink (Dc1m), more light green (Cd3m) compared to dark green (Cd1m), and a greater proportion of yellow (C6m) rather than dark red (C1m). This trend is true for both MY 28 and for the years that followed, but there is also a notable difference seen between these temporal slices. Endmembers with stronger CO_2 ice features (deeper reds of C1m, C3m) are prevalent in MY 28 and there is not a significant proportion of area mapped with slight H_2O ice absorptions (yellow of C6m) until late in the summer. In contrast, subsequent years (MY 29–33) show that C6m is mapped in greater proportions than C1m/C3m across L_S.

These results are in agreement with those presented in Cartwright et al. (2022), but also expand on these temporal trends. In addition to greatly increasing the surface area imaged in each L_S range, the mapping data also expand on the previous L_S 300º cutoff and show spectral variation from L_S 270º onward. This reveals that although south polar terrains at L_S 340–350º in MY 28 had similar endmember expressions to those during L_S 320–330º in the years that followed, this does not represent a simple temporal offset of endmember regime. In other words, the endmember expression seen in MY 28 is not simply shifted back to earlier L_S in subsequent years; there is instead a fundamental difference in how CO_2 ice-rich endmembers are expressed at the surface.

4.3 Residual ice mosaic.

To produce a consistent view of residual ice, we evaluated the temporal extent of endmember C1m (deep red) in Figure 4 and its spatial extent in temporally restricted mosaics. This constrained the L_S cutoff in each year after which there does not appear to be significant seasonal frost on the surface, corresponding to L_S 338º in MY 28, L_S 320º in MY 29, and L_S 310º in MY 30–33; all observations from MY 32 were also cut to remove anomalous mapping of H_2O ice-rich endmembers (likely related to atmospheric conditions). The resulting 180 m/pixel mosaic of MSP and MSW data (Fig. 5) covers ~ 90% of the bright RCD deposits and significant portions of the surrounding PWD and OWD. In this mosaic, the RCD is dominated by a spectral signature of CO_2 ice with weak H_2O ice absorptions (endmember C6m, yellow), though some areas show increased H_2O contributions (Cd3m, pale green). This is consistent with late-summer targeted data from Cartwright et al. (2022) and suggests that even at the coarser resolution of mapping data, sub-pixel contributions from water ice around erosional mesas and other features in the RCD are still visible. However, while targeted data endmember maps had shown ubiquitous expression of CO_2 ice absorptions extending several km beyond the bright exposures of the RCD, expression of these endmembers (pinks of Cw and Dc) are not mapped as consistently between classified mapping strips.

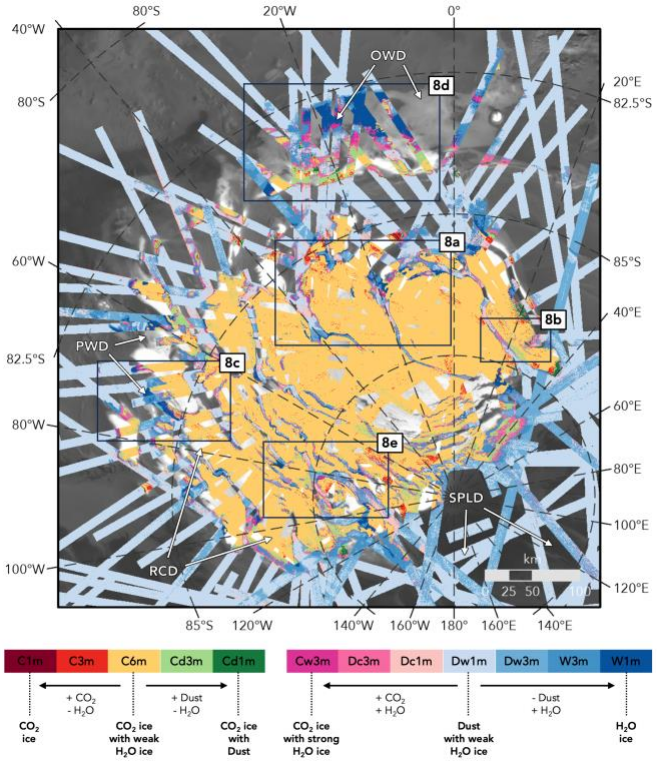

Figure 5. Mosaic showing residual ice exposures with minimal influence from seasonal CO_2 frost. Classified mapping data strips are stacked in ascending order of L_S and compiled from all data acquired after L_S 338° in MY 28, L_S 320° in MY 29, and L_S 310° in MYs 30, 31, and 33. Note the strong agreement between endmember contacts in the mosaic and albedo variations seen in the basemap. Extent indicators are shown for panels in Figure 8.

4.4 Errors and constraints

To constrain how consistently and accurately the random forest classification worked on the mapping dataset, we calculated the spectral variation within each endmember. These statistical envelopes (see Section 3.3.3) include the median spectrum as well as the middle 50% and middle 80% of values at each wavelength. Across endmembers and at the majority of wavelengths, the middle 50% of values are within ±3% of the median and the middle 80% of values are within ±8%. We are therefore confident in the endmember classifications given by the random forest model. In terms of spatial expression, endmember classifications in similarly-timed overlapping observations are in close agreement, meaning that mosaics of narrow L_S ranges show consistent mapping of endmembers across the surface. However, as L_S ranges are expanded or data are aggregated across MYs, there is much greater strip-to-strip variation in endmember expression.

5 Discussion

5.1 Temporal variation

Analyses of CRISM targeted data in Cartwright et al. (2022) revealed several temporal trends in the surface expression of endmembers, the most striking of which being a dominance of CO_2 ice-rich endmembers without H_2O ice contribution across L_S in MY 28 compared to the years that followed. This result was unexpected given that previous studies of thermal and visible data demonstrated that the seasonal CO_2 ice cap had experienced an accelerated retreat following the globe-encircling dust event that occurred during 265° < L_S < 325° of MY 28 (Calvin et al., 2017; Piqueux, Kleinböhl, et al., 2015). If that enhanced retreat were assumed to continue into the interior of the RCD, we would expect to see the addition of weak water ice signatures associated with underlying residual ice revealed at earlier L_S. To instead see sustained CO_2 ice signatures without H_2O ice contribution in the RCD compared to MY 29–33 suggests that these bright CO_2 ice deposits actually experienced a thicker, more prolonged, or otherwise anomalous seasonal cover following the dust event of MY 28. Results from the new mapping data analyses support this story (Fig. 4), but the expanded spatial and temporal coverage offered by the dataset also provides additional context and complexity.

5.1.1 Early southern summer

The mapping data show that the differences in endmember expression between MY 28 and MY29–33 began earlier than the L_S 300º cutoff explored in targeted data and extend at least to the start of southern summer at L_S 270º (Section 4.2; Fig. 4). This finding suggests that the MY 28 dust event did not simply cause a delay in the retreat of seasonal frost from the surface of the SPRC, but instead fundamentally changed the nature of its deposition/removal. It is unclear whether the MY 28 seasonal frost was anomalous because deposition of a thicker frost cover obscured underlying water ice, or because the frost itself did not bear the same water ice contribution seen in other years.

5.1.2 Spatial variation of frost signatures

While the simplified bar plots effectively illustrate seasonal changes in endmember occurrence, the full temporally restricted mosaics are able to show how these changes are expressed spatially. In particular, these mosaics show variations in the retreat of seasonal frost across the SPRC at different times, both within and between MYs (Fig. 6). For example, mosaics from MY 28 display when and where transitions occur from the purest CO_2 ice endmember without significant H_2O ice contribution (deep red C1m) to CO_2 ice-rich endmembers with greater H_2O ice signatures (yellow C6m, green Cd3m). These endmember transitions are most visible at L_S 310–320º where the full breadth of seasonal frost removal can be seen in association with different parts of the SPRC (Fig. 6a). Of particular note are lower elevations of the topographic dome that show extensive exposure of C6m (yellow) and higher elevations where C1m (deep red) is more prevalent. There are even variations in endmember expression on either side of low albedo troughs and slopes that divide RCD exposures (known as dark lanes; e.g., Thomas et al., 2000). These findings are again consistent with the CRISM targeted data maps, but reveal that seasonal frost re-deposition and removal in MY 28 was more complex than previously understood. Specifically, the thickness or longevity of the seasonal cover appears to be influenced by differences in elevation or illumination such that lower elevations experience earlier removal. Alternatively, stronger water ice signatures in some areas could be linked to

local re-deposition of H_2O sublimated from dark lanes (Diniega et al, 2021; Titus et al., 2020). In either case, these compositional variations have important implications for how dust storms and other dynamic processes might affect the mass balance of the RCD and the evolution of south polar topography more broadly.

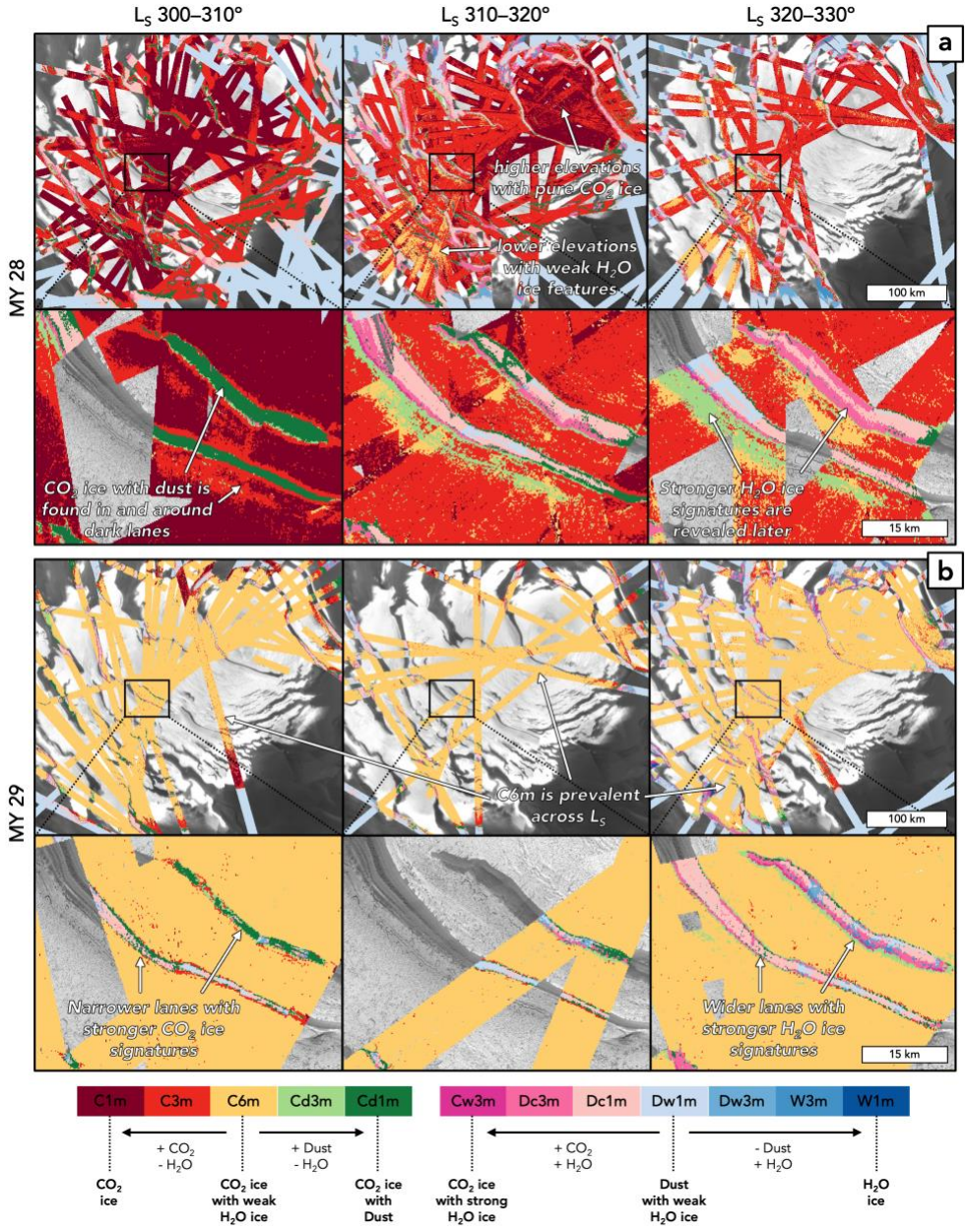

Figure 6. Views of temporally restricted mosaics of classified CRISM mapping data presented in 10° L_S bins over two MYs. **(a)** Endmember progression across MY 28 that shows spatial variations in the exposure of more water ice-rich endmembers over time, likely caused by the removal of seasonal CO_2 frost. **(b)** Variations over the same L_S bins in MY 29 which display a

very different endmember progression dominated by C6m, a CO_2 ice spectrum with minor contribution from water ice. Insets in both panels show details of the mosaics near dark lanes.

5.1.3 Water ice signatures after MY 28

The corresponding L_S-binned mosaics from MY 29 (Fig. 6b) show a very different evolution in endmember expression. Across L_S, the surface of the RCD is dominated by C6m (yellow) while the C1m endmember (deep red) that dominates much of MY 28 is relatively absent. This matches the trends shown in the bar plots in Figure 4 and suggests that there is weak, but consistent contribution from water ice to CO_2 spectra from L_S 270º onwards in MY 29, as well as in the limited windows CRISM sampled in MY 30–33. This is unexpected given that seasonal frost, which previous work has shown to persist until L_S ~330º (Calvin et al., 2017; James et al., 2007; Piqueux, Kleinböhl, et al., 2015), is assumed to have a different spectral signature from underlying residual ice. Instead, frosted and unfrosted surfaces in the endmember maps appear to have identical compositions of CO_2 ice with minor contribution from H_2O.

However, it is important to note that of the 30 candidate mapping data endmembers, six were reclassified to map as C6m. Spectral features within this group do show some variation, but critically, they all display spectral structure around 1.5 µm and a negative slope at ~2.3 µm consistent with the C6 endmember identified in targeted data. And more importantly, these features readily distinguish the C6m spectra from the candidate endmembers reclassified to C1m and C3m (see Fig. S2b in Supporting Information S1). This suggests that there may be a progression from weaker to stronger H_2O ice features in MY 28 captured by the candidate endmembers, but that this progression is subtle enough to not be captured by the simplified 12-endmember set.

There are some notable exposures visible in the MY 29 mosaics that provide additional context to the C6m signature. First, C6m signatures are seen to extend beyond the bounds of the bright residual CO_2 ice at its outer margins and into parts of low-albedo dark lanes, making them appear narrower in classified maps (Fig. 6b). Second, in areas not mapped as C6m such as the interiors of dark lanes, an endmember progression echoing targeted data maps is found: more CO_2 ice- and dust-rich endmembers (shades of green) transition to spectral shapes with weaker CO_2 features (shades of pink) as the summer progresses. Both of these findings confirm that seasonal frost and its removal are being observed in these mosaics. Specifically, the retreat of the seasonal cap can be tracked in areas near the RCD margins unlike in MY 28, where seasonal ice signatures are coincident with the RCD from early on in the summer.

There is existing evidence that seasonal frost may carry a measurable signature of H_2O ice. The north polar seasonal cap has been observed through a variety of thermal and spectral data to have an annulus of water ice as it retreats (Wagstaff et al., 2008; Appéré et al., 2011; Brown et al., 2012). At the south pole, previous work with OMEGA data has shown that "H_2O contamination" of CO_2 frost fluctuates across L_S as the seasonal cap retreats (Langenvin et al., 2007) while Mars Climate Sounder data show that CO_2 snowfall can scavenge H_2O from the atmosphere (Alsaeed & Hayne, 2022). While it is possible that the lack of H_2O ice signatures in MY 28 frost points to a thicker seasonal cap that obscured water contributions in underlying residual ice exposures, the new findings suggest that H_2O usually present in the seasonal cap may have been kept in the atmosphere with dust from the MY 28 storm.

5.2 Residual ice mosaic

5.2.1 Connections to previous work

The mosaic of CRISM mapping observations showing residual ice signatures offers important new context to previous maps of south polar composition (Fig. 7). This view greatly expands on the coverage offered by targeted data maps from Cartwright et al. (2022)(Fig. 7a), which allows the compositional framework presented in that work to be evaluated across an even more diverse set of SPRC terrains. The broadened framework also serves to bridge gaps in understanding between previous THEMIS and OMEGA-derived maps and provide a more comprehensive view than previously possible of the processes that drive the formation and evolution of south polar ices.

Douté et al. (2007) leveraged four OMEGA images covering L_S 335–348º in MY 26 to produce the first comprehensive view of south polar spectral diversity. They used radiative transfer modeling of pixels to separate spectral types in a ternary diagram of CO_2 ice, H_2O ice, and dust content. One of the derived compositional maps is presented in Figure 7c along with a legend that roughly correlates the feature strengths indicated by their model results to the variations observed in CRISM mapping data endmembers. While the dust-to-water-ice transition and expression of residual CO_2 ice are in close agreement between the two datasets (see the interior of the RCD and vast exposures of the SPLD), other spectral types are more difficult to correlate. These compositions are found primarily around the margins of the RCD and in narrow exposures that extend onto the SPLD, further demonstrating that these are some of the most complex and varied ice mixtures in the region. The enhanced spatial resolution of 180 m/pixel offered by CRISM mapping data compared to the ~2 km/pixel provided by OMEGA allows greater detail of compositional variation to be observed in these places. Meanwhile, the increased temporal sampling over several MYs helps to assess which characteristics of the exposures remain constant through time.

A highly detailed map of THEMIS thermal signatures was made by Piqueux et al. (2008) and for the first time mapped the full extent of the OWD. Measured temperatures were used to characterize areas that contain significant CO_2 ice, areas where H_2O ice dominates, and areas with intermediate temperatures indicating some type of mixture. The 100 m/pixel resolution of THEMIS is comparable to the CRISM mosaic and there is very strong agreement between the two datasets in terms of dominant surface composition (Fig. 7d). This is even the case in relatively small and isolated patches of H_2O ice that sit farther from the RCD margins. The CRISM data help to complete this picture by mapping within the THEMIS coverage gap below 87º S, but more importantly, provide new details in spectral variation, particularly in water ice-rich exposures. For example, the amount of dust contributing to different parts of the PWD can be assessed and areas that show more pure water ice can be clearly identified. Additionally, the most extensive areas mapped as generic mixtures by Piqueux et al. (2008) in the OWD are revealed as CO_2 ice with stronger water ice signatures than typical residual cap exposures (shades of green from Cd3m rather than yellow of C6m). These variations indicate that the isolated patches of CO_2 ice that sit atop the OWD are different from the main RCD exposures that sit at higher elevations.

In summary, these three compositional maps have broad agreement in the distribution of basic compositional mixtures. This is clearest in the interior of the RCD, but also extends to the surrounding PWD, where the improved spectral and spatial resolution of CRISM mapping data is

particularly adept at showing the diversity of H_2O ice mixtures with dust and/or CO_2 ice. There is less agreement in the OWD, though this is likely linked to this region's pronounced inter-annual variability in CO_2 frost cover (e.g., Calvin et al. 2017) and the limited ability to make one-to-one comparisons between units/endmembers in the three maps.

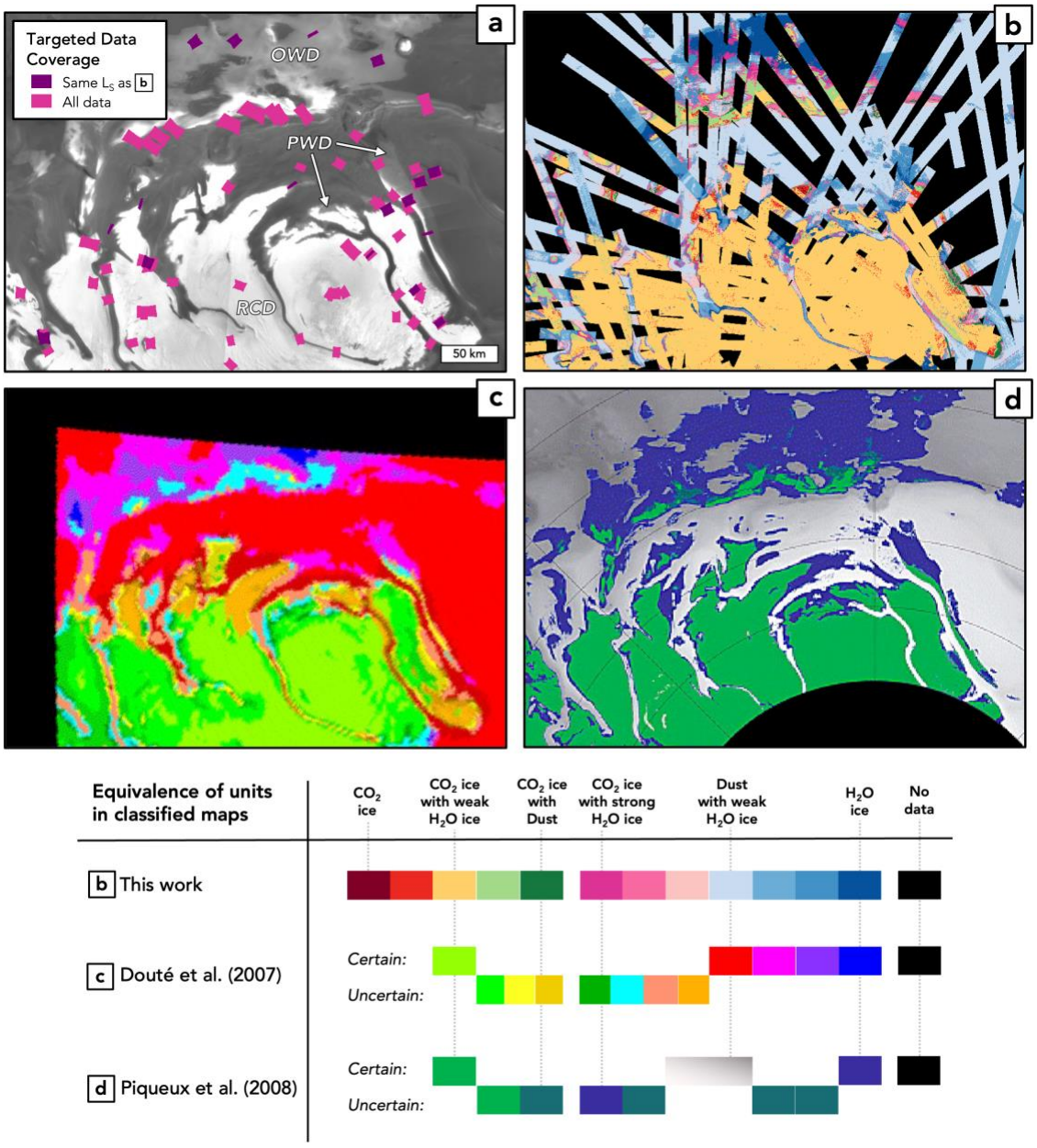

Figure 7. Comparisons of compositional maps of the south polar region. **(a)** Coverage from classified maps of CRISM targeted data from Cartwright et al. (2022) showing all observations vs. those that cover only the same MY and L_S ranges as the mapping data mosaic. **(b)** Mosaic of endmember-classified CRISM mapping data showing exposures of residual ice (i.e., not significantly obscured by seasonal CO_2 frost). **(c)** Classified image from Douté et al. (2007) showing OMEGA orbit 41 (L_S 338º in MY 26). **(d)** Classified image from Piqueux et al. (2008) showing THEMIS temperature data spanning L_S 320°–360°. A hillshade is shown in areas where

552 THEMIS temperatures are interpreted as neither CO_2 nor H_2O ice. The legend gives best-
553 estimate correlations between spectral properties signified by colors in the different maps.

554 5.2.2 Characteristics of major units

555 In the residual ice mosaic, the RCD are mapped primarily as endmember C6m (yellow),
556 indicating CO_2 ice with minor H_2O content (Fig. 8a). However, some areas do show stronger
557 water ice signatures (Fig. 8b) where endmember Cd3m (light green) is mapped around rough
558 erosional morphology and endmembers Dw3m and Dc3m (blue and pink) appear in erosional
559 windows through the RCD. Exposures of the PWD display varying compositions from pure
560 water ice (W1m, deep blue) to more dust (W3m and Dw3m in lighter blues) and even
561 contributions from CO_2 ice (Cw3m, Dc3m in shades of pink). Although water/dust combinations
562 can vary strip-to-strip (e.g., Fig 8c), the outlines of endmember divisions are consistently
563 mapped in these regions. Similarly, the OWD displays a wide variety of compositions such that
564 all 12 endmembers are present (Fig. 8d). These variations closely follow differences in albedo
565 visible in a Mars Orbiter Camera (MOC) mosaic, providing opportunities to study a wealth of
566 contacts between SPLD, OWD, and low-elevation portions of the RCD. Lastly, the SPLD is
567 mapped broadly as endmember Cd1 (pale blue) without the ability to see compositional
568 differences in exposed layers.

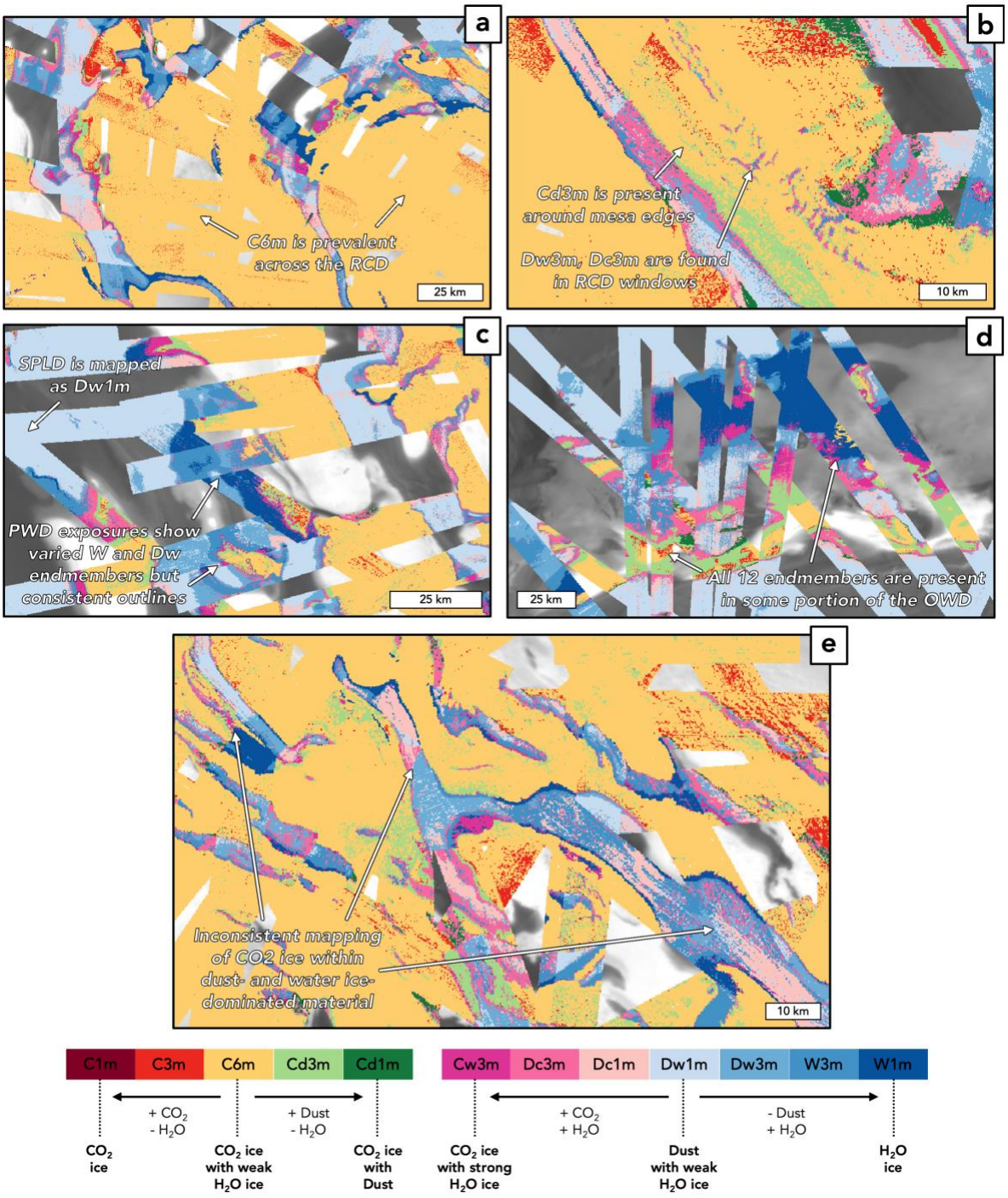

Figure 8. Details of the mosaic showing residual ice surfaces. **(a)** Portions of the RCD showing agreement in residual CO_2 ice signatures. **(b)** A portion of the RCD in which compositional details around erosional features are resolved as more water ice-rich endmembers. **(c)** Exposures of the PWD in which some strips show variable contributions of dust with water ice, but generally follow the same contours on the surface. **(d)** The OWD showing a wide variety of

endmember mappings. **(e)** Detail around dark lanes showing inconsistent mapping of CO_2 ice features with water and dust, expressed as alternating pink and blue classifications.

5.2.3 Variable CO_2 ice signatures

Targeted data showed that dark material surrounding the RCD was almost universally mapped with weak CO_2 ice signatures (shades of pink) across L_S and MYs, even after the removal of apparent seasonal frost. The presence of such a consistent signature indicated that residual CO_2 ice of some kind extends beyond the brightest exposures of CO_2 ice and into surrounding dust- or H_2O ice-dominated deposits. This finding suggests a complex stratigraphy in which layered and unlayered low-albedo material usually presumed to be the SPLD includes some amount of CO_2 ice, which could have implications for how material is introduced into climate records. These same CO_2 ice-bearing exposures are captured by the mapping data results, but are less consistently mapped as evidenced by alternating classification between shades of blue (dust/water ice without CO_2) and shades of pink (also dust/water but with weak CO_2 ice features)(Fig. 8e).

The less consistent expression of weak CO_2 ice features in the mapping data classification is likely caused by the dataset's more limited wavelength sampling and increased spatial binning. Additionally, the random forest model might not be sufficiently sensitive to weak signatures that remain at these lower resolutions. Alternatively, actual CO_2 ice contributions on the surface might be more variable than what is captured by targeted data maps: diurnal, intra-annual, and inter-annual variations could all contribute to the observed variation. In particular, local variations in illumination during the extended days of south polar summer could produce shadowed regions where CO_2 ice accumulates. Depending on the timing of the next overlapping observation several L_S or even MYs later, such shadowed regions could be illuminated again.

6. Conclusions

The new endmember-classified mosaics of CRISM mapping data expand on previous compositional mapping of the SPRC to provide new insights into the dynamic processes that shape this region. Our results and interpretations can be summarized as follows:

- A total of 1103 mapping data strips spanning southern summer of MY 28–33 were processed using a combination of *k*-means clustering and random forest classification. The resulting set of 12 endmembers were found to display spectral signatures consistent with the results of Cartwright et al. (2022), allowing a one-to-one comparison of compositional variation captured by CRISM targeted data and mapping data.
- The classified observations were compiled into a series of temporally restricted mosaics that show how surface composition varies within and between MYs. Importantly, these mosaics allow seasonal variation to be measured within bright exposures of residual CO_2 ice, which is not possible with other datasets covering thermal or visible wavelengths. Consistent with the previous targeted data analyses, CO_2 ice-rich endmembers were found to dominate surface spectra in MY 28. Seasonal retreat in the years that followed was markedly different, potentially with subtle contributions from H_2O ice as early as L_S 270º. This suggests that the large dust event in MY 28 caused either a thicker depositing of seasonal CO_2 frost or a reduction in the amount of H_2O ice contributing to that frost cover.

- By identifying L_S ranges within each MY that did not show significant contribution from CO_2 frost, a mosaic was constructed to show spectral signatures of residual ice deposits. The distribution of ice mixtures is largely consistent with previous OMEGA and THEMIS maps (Douté et al., 2007; Piqueux et al., 2008), but the higher spatial and spectral resolution of CRISM mapping data provides critical new detail. In particular, a greater variety of water ice-rich mixtures can be distinguished compared to THEMIS and their exposure can be resolved in greater detail compared to OMEGA.
- Weak CO_2 ice contributions to dust or H_2O ice-rich mixtures outside the bright residual CO_2 deposits were mapped less consistently in the new mosaics compared to targeted data. This is likely due to the limited spatial and spectral resolution of the mapping data and/or limited sensitivity of the random forest model to these weak features. However, the finding might also point to diurnal or inter-annual variation in CO_2 ice contributions to non-RCD material that is not related to intra-annual trends in seasonal frost removal. This emphasizes the dynamic nature of south polar terrains, where subtle but constant shifts in surface composition can be found, even on exposures of residual ice.
- This work provides a compositional framework that can place the results of Cartwright et al. (2022) into a broader spatial context and aid future studies of south polar composition. For example, constraining the nature of observed mixtures may reveal connections to the formation/evolution of climate records while comparisons of overlapping data will help to track these dynamic processes in detail.

Acknowledgments

This work was made possible through the incredible efforts of the CRISM team and was supported by NASA's Mars Data Analysis Program (80NSSC19K0013). The authors thank Mathieu Vincendon and Sylvain Piqueux for insightful comments that greatly improved the quality of the manuscript.

Open Research

CRISM Targeted Reduced Data Records (TRDRs, Version 3) used in this study are publicly available via the Geosciences Node of the Planetary Data System (Murchie, 2006; Seelos et al., 2023). The derived CRISM endmember spectral library and classified maps are available via a Zenodo repository (Cartwright, 2023). Code written for this study used the open-source Python *scikit-learn* and R *randomForest* libraries (Liaw & Wiener, 2002; Pedregosa et al., 2011). Spatial data were viewed in Esri ArcGIS Pro (Esri Inc., 2020), which is license restricted.

References

Alsaeed, N. R., & Hayne, P. O. (2022). Transport of Water Into the Polar Regions of Mars Through Scavenging by CO_2 Snowfall. *Journal of Geophysical Research: Planets*, *127*(11), e2022JE007386. https://doi.org/10.1029/2022JE007386

Appéré, T., Schmitt, B., Langevin, Y., Douté, S., Pommerol, A., Forget, F., Spiga, A., Gondet, B., & Bibring, J.-P. (2011). Winter and spring evolution of northern seasonal deposits on Mars from OMEGA on Mars Express. *Journal of Geophysical Research: Planets*, *116*(E5). https://doi.org/10.1029/2010JE003762

Arthur, D., & Vassilvitskii, S. (2007). k-means++: The advantages of careful seeding. *Proceedings of the Eighteenth Annual ACM-SIAM Symposium on Discrete Algorithms*, 1027–1035.

Bibring, J.-P., Langevin, Y., Poulet, F., Gendrin, A., Gondet, B., Berthé, M., Soufflot, A., Drossart, P., Combes, M., Bellucci, G., Moroz, V., Mangold, N., Schmitt, B., & OMEGA Team, the. (2004). Perennial water ice identified in the south polar cap of Mars. *Nature*, *428*(6983), Article 6983. https://doi.org/10.1038/nature02461

Bibring, J.-P., Soufflot, A., Berthé, M., Langevin, Y., Gondet, B., Drossart, P., Bouyé, M., Combes, M., Semery, A., Bellucci, G., Formisano, V., Moroz, V., Kottsov, V., Bonello, G., Erard, S., Forni, O., Gendrin, A., Manaud, N., Poulet, F., … Forget, F. (n.d.). *OMEGA: Observatoire pour la Minéralogie, l'Eau, les Glaces et l'Activité*. 13.

Breiman, L. (2001). Random Forests. *Machine Learning*, *45*(1), 5–32. https://doi.org/10.1023/A:1010933404324

Brown, A. J., Calvin, W. M., & Murchie, S. L. (2012). Compact Reconnaissance Imaging Spectrometer for Mars (CRISM) north polar springtime recession mapping: First 3 Mars years of observations. *Journal of Geophysical Research: Planets*, *117*(E12). https://doi.org/10.1029/2012JE004113

Brown, A. J., Piqueux, S., & Titus, T. N. (2014). Interannual observations and quantification of summertime H_2O ice deposition on the Martian CO_2 ice south polar cap. *Earth and Planetary Science Letters*, *406*, 102–109. https://doi.org/10.1016/j.epsl.2014.08.039

Brown, A. J., Calvin, W. M., McGuire, P. C., & Murchie, S. L. (2010). Compact Reconnaissance Imaging Spectrometer for Mars (CRISM) south polar mapping: First Mars year of observations. *Journal of Geophysical Research*, *115*, E00D13. https://doi.org/10.1029/2009JE003333

Byrne, S. (2009). The Polar Deposits of Mars. *Annual Review of Earth and Planetary Sciences*, *37*(1), 535–560. https://doi.org/10.1146/annurev.earth.031208.100101

Calvin, W. M., Cantor, B. A., & James, P. B. (2017). Interannual and seasonal changes in the south seasonal polar cap of Mars: Observations from MY 28-31 using MARCI. *Icarus*, *292*, 144–153. https://doi.org/10.1016/j.icarus.2017.01.010

Cartwright, S. F. A., Calvin, W. M., Seelos, K. D., & Seelos, F. P. (2022). Characterizing Seasonal and Residual Ices at the South Pole of Mars Using a Universal Set of CRISM Spectral Endmembers. *Journal of Geophysical Research: Planets*, *127*(11), e2022JE007372. https://doi.org/10.1029/2022JE007372

Cartwright, S. F. A. (2023). Endmember spectra and classified mosaics derived from CRISM mapping data at the south pole of Mars [Data set]. Zenodo. https://doi.org/10.5281/zenodo.8201616

Christensen, P. R., Jakosky, B. M., Kieffer, H. H., Malin, M. C., McSween, H. Y., Nealson, K., Mehall, G. L., Silverman, S. H., Ferry, S., Caplinger, M., & Ravine, M. (2004). The Thermal Emission Imaging System (THEMIS) for the Mars 2001 Odyssey Mission. *Space Science Reviews*, *110*(1), 85–130. https://doi.org/10.1023/B:SPAC.0000021008.16305.94

Diniega, S., Bramson, A. M., Buratti, B., Buhler, P., Burr, D. M., Chojnacki, M., Conway, S. J., Dundas, C. M., Hansen, C. J., McEwen, A. S., Lapôtre, M. G. A., Levy, J., Mc Keown, L., Piqueux, S., Portyankina, G., Swann, C., Titus, T. N., & Widmer, J. M. (2021). Modern Mars' geomorphological activity, driven by wind, frost, and gravity. *Geomorphology*, *380*, 107627. https://doi.org/10.1016/j.geomorph.2021.107627

Douté, S., Schmitt, B., Langevin, Y., Bibring, J.-P., Altieri, F., Bellucci, G., Gondet, B., & Poulet, F. (2007). South Pole of Mars: Nature and composition of the icy terrains from Mars Express OMEGA observations. *Planetary and Space Science*, *55*(1–2), 113–133. https://doi.org/10.1016/j.pss.2006.05.035

Esri Inc. (2020). ArcGIS Pro Version 2.5 [Software]. Esri Inc. Retrieved from https://www.esri.com/en-us/arcgis/products/arcgis-pro/overview

James, P. B., Thomas, P. C., Wolff, M. J., & Bonev, B. P. (2007). MOC observations of four Mars year variations in the south polar residual cap of Mars. *Icarus*, *192*(2), 318–326. https://doi.org/10.1016/j.icarus.2007.07.014

Kieffer, H. H. (1979). Mars south polar spring and summer temperatures: A residual CO_2 frost. *Journal of Geophysical Research: Solid Earth*, *84*(B14), 8263–8288. https://doi.org/10.1029/JB084iB14p08263

Landis, M. E., Acharya, P. J., Alsaeed, N. R., Andres, C., Becerra, P., Calvin, W. M., Cangi, E. M., Cartwright, S. F. A., Chaffin, M. S., Diniega, S., Dundas, C. M., Hansen, C. J., Hayne, P. O., Herkenhoff, K. E., Kass, D. M., Khuller, A. R., McKeown, L. E., Russell, P. S., Smith, I. B., … Whitten, J. L. (2023). Polar science results from Mars Reconnaissance Orbiter: Multiwavelength, multiyear insights. *Icarus*, 115794. https://doi.org/10.1016/j.icarus.2023.115794

Langevin, Y., Bibring, J.-P., Montmessin, F., Forget, F., Vincendon, M., Douté, S., Poulet, F., & Gondet, B. (2007). Observations of the south seasonal cap of Mars during recession in 2004–2006 by the OMEGA visible/near-infrared imaging spectrometer on board Mars Express. *Journal of Geophysical Research: Planets*, *112*(E8). https://doi.org/10.1029/2006JE002841

Liaw, A., & Wiener, M. (2002). Classification and regression by randomForest. *R News*, **2**(3), 18– 22. Retrieved from https://CRAN.R-project.org/doc/Rnews/

Murchie, S. (2006). *MRO CRISM TARGETED REDUCED DATA RECORD V1.0* [Data set]. NASA Planetary Data System. https://doi.org/10.17189/1519450

Murchie, S., Guiness, E., and Slavney, S. (2016). CRISM Data Product Software Interface Specification, Version 1.3.7.4. https://pds-geosciences.wustl.edu/mro/mro-m-crism-2-edr-v1/mrocr_0001/document/crism_dpsis.pdf

Murchie, S., Arvidson, R., Bedini, P., Beisser, K., Bibring, J.-P., Bishop, J., Boldt, J., Cavender, P., Choo, T., Clancy, R. T., Darlington, E. H., Des Marais, D., Espiritu, R., Fort, D., Green, R., Guinness, E., Hayes, J., Hash, C., Heffernan, K., … Wolff, M. (2007). Compact Reconnaissance Imaging Spectrometer for Mars (CRISM) on Mars Reconnaissance Orbiter (MRO). *Journal of Geophysical Research*, *112*(E5), E05S03. https://doi.org/10.1029/2006JE002682

743 Murray, B. C., Soderblom, L. A., Cutts, J. A., Sharp, R. P., Milton, D. J., & Leighton, R. B.
744 (1972). Geological framework of the south polar region of Mars. *Icarus*, *17*(2), 328–345.
745 https://doi.org/10.1016/0019-1035(72)90004-8

746 Pedregosa, F., Varoquaux, G., Gramfort, A., Michel, V., Thirion, B., Grisel, O., Blondel, M.,
747 Prettenhofer, P., Weiss, R., Dubourg, V., Vanderplas, J., Passos, A., Cournapeau, D.,
748 Brucher, M., Perrot, M., & Duchesnay, É. (2011). Scikit-learn: Machine Learning in
749 Python. *The Journal of Machine Learning Research*, *12*(null), 2825–2830.

750 Piqueux, S., Byrne, S., Kieffer, H. H., Titus, T. N., & Hansen, C. J. (2015). Enumeration of Mars
751 years and seasons since the beginning of telescopic exploration. *Icarus*, *251*, 332–338.
752 https://doi.org/10.1016/j.icarus.2014.12.014

753 Piqueux, S., Edwards, C. S., & Christensen, P. R. (2008). Distribution of the ices exposed near
754 the south pole of Mars using Thermal Emission Imaging System (THEMIS) temperature
755 measurements. *Journal of Geophysical Research: Planets*, *113*(E8).
756 https://doi.org/10.1029/2007JE003055

757 Piqueux, S., Kleinböhl, A., Hayne, P. O., Kass, D. M., Schofield, J. T., & McCleese, D. J.
758 (2015). Variability of the martian seasonal CO_2 cap extent over eight Mars Years. *Icarus*,
759 *251*, 164–180. https://doi.org/10.1016/j.icarus.2014.10.045

760 Plaut, J. J., Picardi, G., Safaeinili, A., Ivanov, A. B., Milkovich, S. M., Cicchetti, A., Kofman,
761 W., Mouginot, J., Farrell, W. M., Phillips, R. J., Clifford, S. M., Frigeri, A., Orosei, R.,
762 Federico, C., Williams, I. P., Gurnett, D. A., Nielsen, E., Hagfors, T., Heggy, E., …
763 Edenhofer, P. (2007). Subsurface Radar Sounding of the South Polar Layered Deposits of
764 Mars. *Science*, *316*(5821), 92–95. https://doi.org/10.1126/science.1139672

765 Prettyman, T. H., Feldman, W. C., & Titus, T. N. (2009). Characterization of Mars' seasonal
766 caps using neutron spectroscopy. *Journal of Geophysical Research: Planets*, *114*(E8).
767 https://doi.org/10.1029/2008JE003275

768 Seelos, F. P., Seelos, K. D., Murchie, S. L., Novak, M. A. M., Hash, C. D., Morgan, M. F.,
769 Arvidson, R. E., Aiello, J., Bibring, J.-P., Bishop, J. L., Boldt, J. D., Boyd, A. R.,
770 Buczkowski, D. L., Chen, P. Y., Clancy, R. T., Ehlmann, B. L., Frizzell, K., Hancock, K.
771 M., Hayes, J. R., … Wolff, M. J. (2023). The CRISM investigation in Mars orbit:
772 Overview, history, and delivered data products. *Icarus*, 115612.
773 https://doi.org/10.1016/j.icarus.2023.115612

774 Smith, I. B. (2022). A Retrospective on Mars Polar Ice and Climate. In I. B. Smith, *Oxford*
775 *Research Encyclopedia of Planetary Science*. Oxford University Press.
776 https://doi.org/10.1093/acrefore/9780190647926.013.242

777 Thomas, P. C., Calvin, W., Cantor, B., Haberle, R., James, P. B., & Lee, S. W. (2016). Mass
778 balance of Mars' residual south polar cap from CTX images and other data. *Icarus*, *268*,
779 118–130. https://doi.org/10.1016/j.icarus.2015.12.038

780 Thomas, P. C., Malin, M. C., Edgett, K. S., Carr, M. H., Hartmann, W. K., Ingersoll, A. P.,
781 James, P. B., Soderblom, L. A., Veverka, J., & Sullivan, R. (2000). North–south
782 geological differences between the residual polar caps on Mars. *Nature*, *404*(6774),
783 Article 6774. https://doi.org/10.1038/35004528

784 Titus, T. N., Kieffer, H. H., & Christensen, P. R. (2003). Exposed Water Ice Discovered near the
785 South Pole of Mars. *Science*, *299*(5609), 1048–1051.
786 https://doi.org/10.1126/science.1080497

787 Titus, T. N., Williams, K. E., & Cushing, G. E. (2020). Conceptual Model for the Removal of
788 Cold-Trapped H_2O Ice on the Mars Northern Seasonal Springtime Polar Cap.
789 *Geophysical Research Letters*, *47*(15), e2020GL087387.
790 https://doi.org/10.1029/2020GL087387

791 Viviano, C. E., Seelos, K. D., Phillips, M. S., Cartwright, S. F. A., Beck, A. W., Seelos, F. P.,
792 Murchie, S. L., Dapremont, A. M., Frizzell, K. R., & Smith, I. B. (2020). *Regional*
793 *compositional mapping using CRISM multispectral mapping data.* 51st Lunar and
794 Planetary Science Conference, Houston, TX.
795 https://www.hou.usra.edu/meetings/lpsc2020/pdf/1485.pdf

796 Viviano-Beck, C. E., Seelos, F. P., Murchie, S. L., Kahn, E. G., Seelos, K. D., Taylor, H. W.,
797 Taylor, K., Ehlmann, B. L., Wiseman, S. M., Mustard, J. F., & Morgan, M. F. (2014).
798 Revised CRISM spectral parameters and summary products based on the currently
799 detected mineral diversity on Mars: REVISED CRISM SUMMARY PRODUCTS.
800 *Journal of Geophysical Research: Planets*, *119*(6), 1403–1431.
801 https://doi.org/10.1002/2014JE004627

802 Wagstaff, K. L., Titus, T. N., Ivanov, A. B., Castaño, R., & Bandfield, J. L. (2008). Observations
803 of the north polar water ice annulus on Mars using THEMIS and TES. *Planetary and*
804 *Space Science*, *56*(2), 256–265. https://doi.org/10.1016/j.pss.2007.08.008